Optimization of Dedicated Scintimammography Procedure Using Detector Prototypes and Compressible Phantoms

S. Majewski [1], D. Kieper[1], E. Curran[1,3], C. Keppel[1,4], B. Kross[1], A. Palumbo[1,3], V Popov[1], A.G. Weisenberger[1,3], B. Welch[1], R. Wojcik[1]

M.B. Williams[2], A. R. Goode[2], M. More[2], G. Zhang[2]

[1] Thomas Jefferson National Accelerator Facility, Newport News, Virginia, 23606

[2] Department of Radiology, University of Virginia, Charlottesville, Virginia, 22908

[3] New Horizons Governor's School for Science and Technology, Newport News, Virginia, 23666

[4] Department of Physics, Hampton University, Hampton, Virginia, 23668

Abstract

Results are presented on the optimization of the design and use of dedicated compact scintimammography gamma cameras. Prototype imagers with a field-of-view (FOV) of 5cm x 5cm, 10cm x 10cm and 15cm x 20cm were used in either a dual modality mode as an adjunct technique to digital x-ray mammography imagers or as stand-alone instruments such as dedicated breast SPECT and planar imagers. Experimental data was acquired to select the best imaging modality (SPECT or planar) to detect small lesions using Tc^{99m} radio-labeled pharmaceuticals. In addition, studies were performed to optimize the imaging geometry. Results suggest that the preferred imaging geometry is planar imaging with two opposing detector heads while the breast is under compression, however further study of the dedicated breast SPECT is warranted.

I. INTRODUCTION

Scintimammography studies performed with standard nuclear medicine cameras suffer from poor sensitivity for lesions under 1cm in diameter and lesions located in the medial aspect of the breast [1, 2, 3]. Several independent groups have been working to explore various technologies to develop compact imagers optimized for scintimammography. The compact design of these detectors greatly improves the imaging geometry and allows various image orientations. The technologies used include position sensitive photomultiplier tubes (PSPMTs), photodiodes, and cadmium-zinc-telluride (CZT) detectors. Compact gamma cameras based on PSPMTs are being used by several groups [4, 5, 6]. Patient studies employing dedicated planar PSPMT systems demonstrate promising advantages over the standard camera technique and these results have sparked commercial interest [7, 8]. Photodiode systems are being utilized and have also been implemented by commercial partners [9]. Finally, CZT based systems hold great promise and continue to develop with the advances in that technology [10]. In addition to scintimammography applications, compact detectors have been developed for positron emission mammography [11, 12, 13, 14].

Dedicated breast SPECT imaging has been proposed and may hold promise with further study [15]. In theory, SPECT reconstruction projections would improve lesion to background contrast ratios. Limited studies have been conducted with a CZT based SPECT system [10]. Studies performed with conventional cameras to compare planar and. SPECT imaging modalities demonstrate the technical challenges of scintimammography [16].

In collaboration with several partner institutions, we have been working with PSPMT based imagers in several modalities in an effort to find the best clinical solution for metabolic radionuclide imaging of the breast. Our involvement with both single gamma and positron detection has permitted several configurations for our systems in both patient and phantom studies with a specialized elastic breast phantom. The patient studies included scintimammographic planar imaging (6"x 8" detector), scinti/digital mammography dual modality imaging (4"x 4" detector), and gamma imaging for stereotactic guided biopsy (2"x 2" detector) [17, 18]. We have recently also obtained preliminary data for a dedicated breast SPECT system based on a PSPMT design.

II. DETECTOR DESIGN AND PERFORMANCE

A. Detector System

We have constructed several mini gamma camera prototypes based on an array of compact Hamamatsu [19] R7600-00-C8 position sensitive photomultiplier tubes (PSPMTs). Figure 1 shows a schematic diagram of the 20cm x 15cm mini gamma camera detector head.

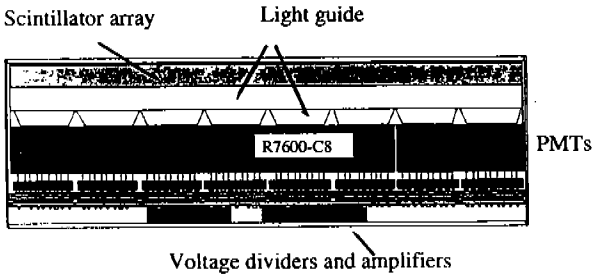

Figure 1: Schematic of the detector head made of an array of 8x6 R7600-00-C8 PSPMTs. (Collimator and tungsten shield are not shown.)

Each of the R7600-00-C8 PSMTs has a transversal size of 26 x 26 mm^2 and a minimum effective photocathode area of 22 x 22 mm^2. The 8 x 6 PSPMT array was optically coupled to a high quality matching size pixellated NaI(Tl) array

manufactured by Bicron Corporation [20]. The array is a matrix of ~3 mm x ~3 mm x 6 mm crystals encapsulated in a compact housing with a 5 mm thick glass window which acts as the first part of the two-component optical coupling window (Figure 2).

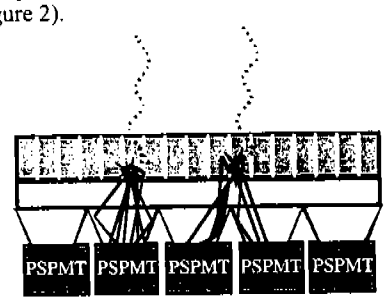

Figure 2: Tapered light guides are used to bypass the dead regions between individual PSMTs in the PSMT array.

Each NaI(Tl) pixel element is separated by 0.3 mm septa made of diffusing white epoxy (see Figure 3). An intrinsic energy resolution of 8.5% FWHM @122 keV was measured for this array using a standard PMT. The second part of the optical window is made of a series of individual tapers to facilitate a uniform response across the surface of the detector array despite the dead regions between individual PSPMTs.

An in-house built multi-electrode amplifier circuit was used to combine the individual anode signals from all of the PSPMTs. For example, in the 8" x 6" camera this resulted in a total of 32 outputs (18 for x-direction and 14 for y-direction). Two data acquisition systems were used. The first was based on an Apple Macintosh G3 attached to a mini-CAMAC crate with two 16ch FERA LeCroy ADCs. The second was built around a PC computer with two 16 channel Datel PCI ADC cards. In both cases the software program Kmax from Sparrow Inc. was used to control the acquisition [21]. The average energy resolution, including all the uniformity corrections (PSPMT response, light guide response, dead area losses, etc), was 17.5% FWHM at 140 keV.

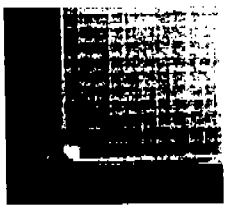

Figure 3: A photographic zoom of the corner region of the 8"x6" NaI(Tl) crystal array. Note the minimized dead space at the bottom edges (chest wall side).

B. Data Acquisition and Detector Calibration

The data acquisition software was developed with the Sparrow Corporation Kmax development system. The control software generates an image by processing the raw anode data event by event. Determination of the position of gamma-ray interaction in the scintillator element is determined by computing a truncated center of gravity of the signal distribution on the X and Y anodes of the PSPMT array. The calculation of the center of gravity is achieved by using only the digitized signals of those anode wires in the calculation that have a predefined chosen optimum fraction of the sum of the anode signals (typically 5 to 10%). We have found that the use of this truncated, center-of-gravity (COG) technique is essential to maximizing use of the PSPMT array [6]. The X and Y value results of the X and Y COG calculations are used to locate which crystal of the array scintillated. At this time the sum of all the X and Y anode signals is used to determine if the scintillation event was in the chosen energy window. Each crystal has defined a separate energy acceptance window. The final processed image is formed by incrementing each pixel corresponding to the crystal element.

The calibration of the detector system consists of four normalization routines (pedestal buffer, crystal mapping, energy calibration and flood correction). The pedestal buffer routine determines the baseline voltage value for each of the data channels and corrects the sampled base line value to zero. Once this correction has been made, each scintillation event recorded by the data channel readout is plotted in a two dimensional histogram (image raw) where the X, Y position of each event is determined by the truncated COG calculation mentioned above. Light emission from each of the crystals in the pixellated scintillator illuminates a small region of the PSPMT array. For each of the crystals in the array, there is an area of pixels in the image raw representing the peak region of light output, COG, shown in Figure 4.

Figure 4: Left: A four PSPMT region of the raw image obtained with a Na^{22} source. Each scintillator pixel is well separated. Note the spatial distortion due to the combined effects of the dead regions between the PSPMTs and the non uniformity of gain characteristics of the individual photomultipliers. Right: A Corrected image of the same region.

By using a high-energy gamma source, Na^{22}, to obtain a high event signal amplitude, the separation of the COGs can be optimized. A high statistics flood using Na^{22} is obtained and the flood image is then processed by a crystal mapping routine. In the crystal mapping routine, a region-of-interest (ROI) is placed around each of the COGs in the image raw until each crystal in the array has an ROI. The resulting lookup table grid is stored in software and is used to sort the scintillation events into the appropriate crystal data bin.

The energy response correction is the next step in detector calibration. This routine allows a pixel-by-pixel energy correction to correct for PSPMT and light collection inefficiencies. Energy spectra are recorded for each of the data bins in the crystal map. The photopeak location for each crystal is recorded and multiplied by a normalization factor. The resulting normalization factors are stored as an energy lookup table. During an actual image acquisition, all of the preceding corrections are applied and the corrected data is displayed in a two dimensional histogram termed the image full. An energy window is added as a sort condition in the image full to eliminate noise and scatter events from the image. Finally, a high statistics uniformity flood is obtained

and the average number of counts from all of the data bins of the image full is divided by the number of counts in each bin to calculate a uniformity correction value for every bin in the image to flatten the image.

C. Collimator Sensitivity and Resolution

Several collimators were available for the study and their mechanical parameters are listed in Table 1. The collimators represent a range of collimator types from high efficiency to high resolution. Four of the collimators were of a corrugated lead construction and one was an etched tungsten design with square holes, from Thermo Electron - Tecomet [22]. The collimator sensitivity was evaluated using a 10 cm diameter petri dish filled with 151 μCi of Tc^{99m} distributed in 3 mm deep solution. The disk was placed directly on the collimator and counts were obtained for 2 minutes. All sensitivity measurements are corrected for radioactive decay and are based on both a +/- 10% energy window and the current operating energy window for the system of –2.5%, +30%. Results for the collimators using the +/-10% energy window condition are shown in Figure 5.

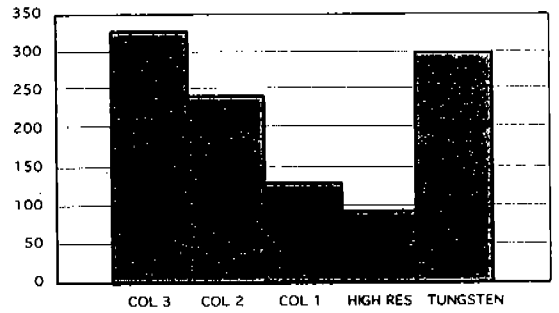

Figure 5: Comparative sensitivity measured for five selected collimators for +/-10% energy window.

It should be noted that collimators 1, 3 and tungsten collimator were positioned about 0.5 cm above the surface of the scintillator array. The two energy window measurements demonstrated differences in counting efficiency because of the system energy resolution. Measured values for each of the imaging energy windows is included in Table 2.

Table 1: Collimator parameters.

	Hole Diameter (mm)	Height (mm)	Septa (mm)
Collimator 1	1.397	27.000	0.203
Collimator 2	1.575	21.006	0.267
Collimator 3	1.778	19.99	0.305
High Res.	1.243	27.904	0.241
Tungsten	1.25 Square	17.8	17.8

Table 2: Measured collimator sensitivity for two imaging energy windows.

	-/+10 %WINDOW	-2.5,+30% WINDOW
Collimator 1	131cpm/μCi	99cpm/μCi
Collimator 2	242cpm/μCi	178cpm/μCi
Collimator 3	328cpm/μCi	244cpm/μCi
High Res.	93cpm/μCi	72 cpm/μCi
Tungsten	299cpm/μCi	220cpm/μCi

The expected values are derived from a method suggested by collimator manufacturers (with an expected transmission correction factor of 0.71). This normalization has been developed empirically and provides good agreement with measured values in standard Anger cameras. The measured sensitivity for the collimators averaged 54.5% of the expected value. The loss of sensitivity is because of a number of known complications of pixellated arrays. First, the septal walls separating adjacent pixels result in a loss of 18% of the active surface area. The second factor effecting the sensitivity relates to energy resolution, as seen in Table 2. Standard cameras average about 10% energy resolution while our system has an energy resolution of 17%. This wider energy resolution of the pixellated system results in fewer counts in the standard +/-10% energy window. This effect alone reduces the measured counts by 23%. Lastly, the crystal depth of 6 mm has an 80% stopping power for the 140 KeV gamma-ray photon. This results in an additional 15% loss of efficiency when compared to the commercial detector's 95% stopping power.

The combined effect of these three factors accounts for a 40% loss of efficiency for the detector system. These calculations still do not entirely account for the difference between the measured and expected values. The remaining gap is possibly because of the inefficiency of scintillation events occurring near the edge of the pixel. The probability of the escape electron re-depositing all of its kinetic energy in the crystal structure decreases at the edge of the crystal [23]. Since the pixellated crystal array is made of many small individual crystal elements the probability of a scintillation event occurring at the edge of a crystal is obviously much higher than for a solid crystal. A near-future simulation study is planned to finalize the sensitivity analysis.

Next system spatial resolution was measured for the same five collimators. Each collimator measurement was performed with two capillary tubes mounted on a translation table. Resolution was measured for distances ranging from 1 to 15 cm from the collimator face. Results are shown in Figure 6.

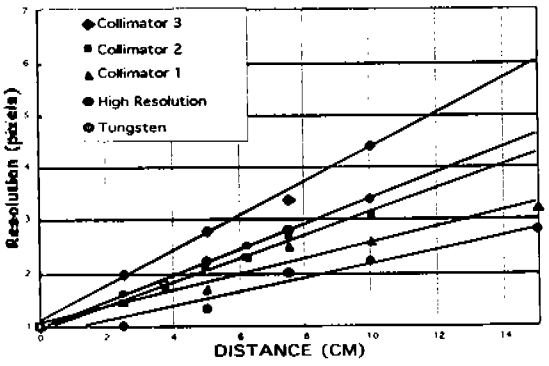

Figure 6: System resolution with various collimators. Each of lines represents a linear fit through the data points. Vertical scale is in scintillation pixels (1 pixel = 3.3 mm).

The resolution and efficiency measurements conducted indicate the standard inverse relationship between the two parameters for the four lead collimators. The tungsten collimator, however, proved to have a slight advantage over its lead counterparts, experiencing better resolution for equivalent sensitivity. Resolution for this collimator closely matched that measured with collimator number 2 from the lead series, while it possessed a 24% higher sensitivity. The practical use of the tungsten collimator may be limited since its cost is several times that of a lead collimator.

To provide optimal sensitivity with a good spatial resolution of 5 mm FWHM at 5 cm, lead collimator #3 was chosen for most of the non-SPECT studies. The compressed geometry used in these studies reduces the maximum tumor-to-detector distance to 5 cm. The system spatial resolution at this distance suffers less from intrinsic collimator resolution so sensitivity is the proper parameter for optimization. Collimator #2 was selected for the SPECT scans as these studies require good resolution at a distance up to 12 cm from the detector.

III. PHANTOM STUDIES

A. Compressible Phantom Preparation

An important technical aspect of the study was our ability to perform comparative imaging of the same elastic breast phantoms with compressions ranging from 10 cm to 5 cm, in both planar and SPECT imaging geometry. The flexible breast phantoms consisted of four main parts: a plastic chest wall back plate, a latex outer skin, a gelatin core and plastic lesions [24]. To prepare the phantom, the latex skin is first washed and treated with optical grease to make the skin transparent for visual inspection. The shape is then formed utilizing a hard plastic breast mold attached to a vacuum pump. A seal is formed around the open chest wall side of the mold, and the vacuum pump pulls the latex down into the form. Next, gelatin and water are combined in a mixing container and the mixture is heated to the gelatin melting point. This heated mixture is placed on a magnetic stir plate and Tc^{99m} is added during stirring. The resulting solution is poured into the formed skin.

The entire molding system is then placed into an ice bath. The ice bath decreases cooling time and causes the mixture to gel from the breast wall inward. This wall-to-center cooling process is paramount for good lesion placement. While the mixture cools, three hollow plastic lesions (volumes 1.0 ml, 0.6 ml and 0.35 ml) are prepared with a specific activity typically six times greater than the gelatin breast. Once the breast solution has solidified to 50%, the lesions are inserted using a pair of hemostats. The 50% gel level allows insertion through the warm liquid layer into the gel layer without causing any tears in the gel structure. After the entire breast volume has solidified, the plastic back plate is attached to the chest wall side of the breast and the assembly is removed from the mold. The back plate is an oval piece of 5 mm thick plastic with a center mounted pivot rod to facilitate mounting to the SPECT drive train. The resulting phantom can be imaged in a compressed or uncompressed geometry and regains the original shape and lesion location once released from compression.

B. Torso Phantom

Human bio-distribution of the imaging agents must be considered for practical breast imaging. Internal organs such as the heart and liver have specific activities significantly above the breast tissue. To evaluate the effect of scattered photon background we utilized an anthropomorphic torso phantom [25] in conjunction with the breast phantoms described above. Typical organ activities were determined using bio-distribution data obtained via pharmaceutical uptake studies [26, 27]. The anthropomorphic phantom consists of several chambers arranged to simulate internal organ geometry. Each of the chambers was filled with a Tc^{99m} solution to provide proper absolute values and concentration ratios for each of the organs, as listed in Table 3. To provide for additional imaging time, the specific activity of all organs was sometimes uniformly increased. All organ-to-breast ratios however were maintained.

Table 3: Typical specific activities and filling ratios for various organs, as used in the phantom studies with the torso phantom.

Organ	Concentration (μCi/ml)	Ratio Organ:Breast
Heart	1	3.0
Liver	3.9	11.8
Lung	0.51	1.5
Torso	0.33	1
Breast	0.33	1
Lesion	2	6.1

During the preliminary evaluations, it was confirmed that scattering in breast of gamma rays emitted by internal organs effected image contrast, especially in the breast region closest to the chest wall, and required scatter reduction or elimination to maximize image quality. However, the effect was small when using the above anthropomorphic torso phantom (see Figure 7a). Therefore, to amplify the scatter effect, additional scatter rejection studies were conducted using the multi-lesion box breast phantom with a fillable 5x5x1 inch flood phantom placed along the "chest wall" side of the detector, in lieu of the torso phantom. The activity of the flood phantom was increased from 1 to 5 mCi over a series of measurements to evaluate image quality under high intensity scatter conditions. The torso and flood phantom studies were conducted using two identical 4"x4" detector heads: one with the Bicron NaI(Tl) array and one with the CsI(Tl) array of 3x3x3mm pixels from Hilger Crystals [28]. One of the obtained comparative results is shown in Figure 7b. The obvious difference in scatter rejection capability close to the chest wall between the two scintillator choices is primarily due to poorer energy resolution of the CsI(Tl) arrays (>30%). All further testing was limited to the NaI(Tl) arrays in which case the impact of scatter even under these extreme conditions was minimal.

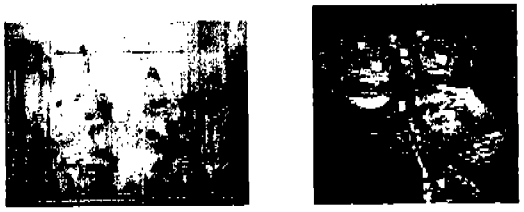

Figure 7a: Left: Top view of the multi-lesion breast box phantom. Right: View of the phantom attached to the torso during imaging session. Small gamma camera is placed below the phantom.

Figure 7b: Left: 5 minute CsI(Tl) detector unfiltered image of the multi-lesion breast box phantom with the high intensity flood phantom ("hot torso") against bottom edge. Right: NaI(Tl) detector image under identical conditions.

C. Phantom Study Results

Two imaging modalities were compared using flexible, compressible breast phantoms made from gelatin with inserted small fillable lesions. Typically, three lesion sizes (volumes) were chosen: of 0.35 ml, 0.6 ml and 1 ml. Several uptake ratios between the lesion and the surrounding "healthy" breast tissue from 3:1 to 6:1 were used. In the first modality, breast phantom was under compression down to ~5 cm for a 10-minute acquisition. In addition, the dedicated breast SPECT imaging modality was evaluated with the uncompressed breast phantom (~10 cm cross section).

Planar Imaging

Figure 8 demonstrates the basic experimental setup for the compression planar tests and presents the theoretically optimal dual detector system. The test system was equipped with the highest sensitivity collimator #3 (see Table 2 and figures 4 and 5) to maximize image statistics. The consequential system resolution loss was acceptable since the imaging geometry under compression requires an effective field depth of only a few centimeters. Examples of the results of planar imaging for the compressed and non-compressed breast phantom are shown in Figures 9-11 and in Table 4. Figure 9 shows the energy spectrum and the uniformity-corrected but unfiltered image for the compressed breast phantom from figure 8. To simulate dual head system, the breast phantom was imaged from both sides using the same detector head. The results of table 4 show that proximity to lesion is almost as important as compression in detecting small lesions. A combination of attenuation, scatter, and resolution, each resulting in fractional losses, combine to produce significant signal reduction as a function of tumor-to-detector distance.

To experimentally evaluate this effect, a simple box phantom was filled with water to a height

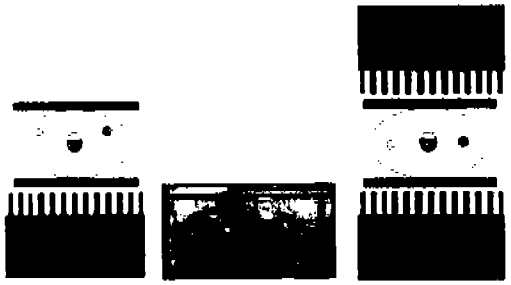

Figure 8. The left schematic drawing shows the imaging geometry with breast phantom under compression. Several lesions of different sizes and the uptake ratios (typically 6:1) were used. Middle photograph shows the actual gelatin phantom under compression. The second schematic drawing at right illustrates the preferred imaging geometry with breast under compression and two detector heads

of 10cm and a 9mm diameter lesion filled with 25μCi of Tc^{99m} solution was mounted to an adjustable height platform immersed in water. An ROI placed directly around the lesion region in the reconstructed image provided a regional count sort condition to measure count rate depedence on distance (water layer thickness). Lesion signal was evaluated at distances of 0, 2.5, 5 and 7.5cm and an energy spectrum within the ROI encompassing lesion at each distance was also recorded.

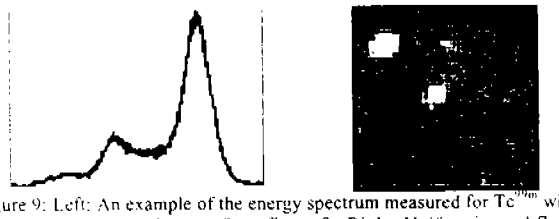

Figure 9: Left: An example of the energy spectrum measured for Tc^{99m} with a compressed breast phantom from figure 8. Right: Uniformity and flood corrected non-filtered image of the same phantom using a -2.5%-to-+30% energy window around the center of photopeak.

The number of counts within an energy window of -2.5 to +30% of the photopeak was obtained from these ROI generated energy spectra (see Figure 12). Approximately exponential change in lesion signal intensity with distance, reaching almost factor 2 at a distance of 5 cm, agrees with expectations and the analysis devoted to breast imaging in Weinberg et al. [29]. Attenuation coefficient of 0.130/cm obtained in the exponential fit to the data points in figure 12 agrees well with the quoted there value of attenuation coefficient of 0.125/cm for tissue. This result confirms the importance of minimizing distance to the lesion and not only thickness of the overlaying tissue.

R. Pani et al. recently suggested [30] that a local minispot compression can be used to achieve higher compression factor and, therefore, to increase contrast obtained with small lesions (or lesions with lower uptake ratios). To study this idea, a gelatin phantom was prepared with three lesions: 0.35 ml with 6:1 uptake ratio, 0.6ml with 6:1 uptake ratio and a 0.35 ml with 3:1 uptake ratio. First a usual planar image was obtained with uniform 5cm compression. Then using a 45mm diameter mini compression paddle a 2.5cm compression was locally applied only in the region of a 0.35

ml lesion with 3:1 uptake ratio. Figure 13 demonstrates improved contrast of that lesion in the latter case. While this result confirms that better visualization of small lesions is possible, this method can be only used if an a priori knowledge of the lesion location is available.

Table 4: S/N and Contrast values for the smallest 0.35 ml lesion from figure 8. S/N (signal to noise) = $(N_L-N_B)/sqrt{N_L}$, CONTRAST= $100\%*(N_L-N_B)/N_B$). The highest contrast and S/N values were obtained for the compressed case with the imaging from the close to lesion side.

Imaging Case	S/N	CONTRAST(%)
Compressed -Bottom View	7.79	15
Non-compressed-Bottom View	6.85	10
Compressed-Top View	17.13	36
Non-compressed Top view	15.04	26

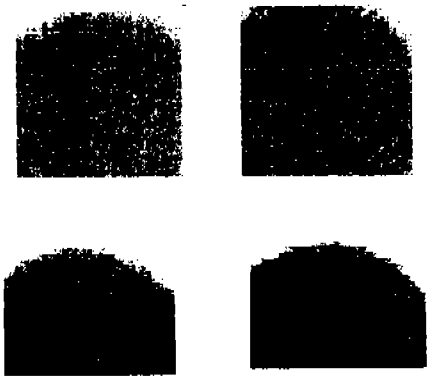

Figure 10: Images obtained from both sides of the same phantom under 5cm compression (top) and under no compression (bottom). The 0.35ml lesion is for seen at the top left of the top left compression image and at the top right (vertical mirror reflection) of the right top image. The top compression images demonstrate the effect of distance on the detection of the smallest 0.35 mm lesion. The bottom images show the same situation, but under no compression.

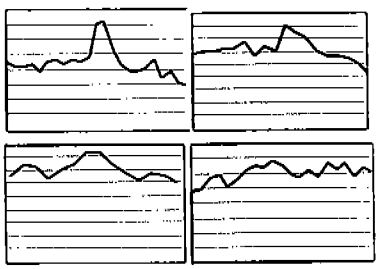

Figure 11: Profile histograms through the small 0.35 ml lesion in the phantom images from figure 10 taken in the same order (top: compressed-close to lesion side, compressed-far to lesion side, bottom: non-compressed-close, non-compressed-far).

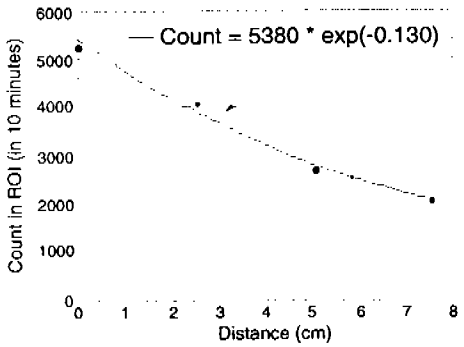

Figure 12: Dependence of detection sensitivity, expressed in counts per 10 minutes within lesion ROI as a function of lesion distance from detector (in cm). Hot 9mm diameter lesion in a cold breast phantom filled with water was used.

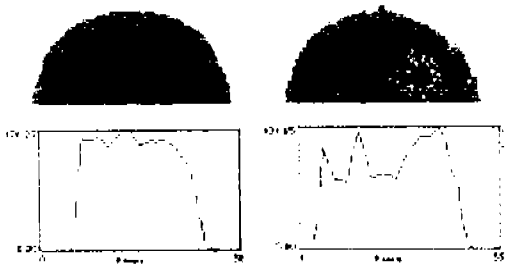

Figure 13: Effect of a locally applied strong compression on contrast of a 0.35ml lesion with a 3:1 uptake ratio. Left: 5 cm uniform compression (top) and a vertical profile through this lesion (bottom). Right: 2.5cm local compression applied in the lesion region with the obtained image at top and the corresponding vertical profile at bottom. Note substantial increase in contrast under mini-spot compression.

SPECT Studies

In order to test the SPECT concept we used a computer controlled stepper motor mounted from a gantry to allow the breast phantom to be pendent and rotated about an axis (see figure 14). The acquisition software was modified to automate the step and shoot process. Several acquisition parameters were adjusted and optimized during the original studies. A 180° acquisition was evaluated for effectiveness and it was found to lack the ability to reconstruct focal hotspots for all of the lesions within the phantom. This is most likely due to the lesion proximity limitation discussed in the planar section above.

Figure 15 shows an example of the SPECT reconstruction obtained utilizing the 8"x6" field-of-view camera system with a general-purpose collimator (#2 from Table 2). The gelatin breast phantom with three hollow plastic lesions (1.0 ml, 0.6 ml and 0.35ml) was prepared with a 6:1 lesion-to-background ratio. Imaging time was statistically equivalent to a 0.7 minute per step acquisition time for a patient breast background activity of 0.3μCi/ml. This imaging time was selected to determine the clinical practicality of a three-head dedicated SPECT instrument. The total imaging time for the proposed three-head study would be under 25 minutes (107 steps over 360°). Prior to SPECT reconstruction, raw image data was processed by a dilation/bilinear interpolation algorithm followed by a 3x3 median smooth. Image

reconstruction provides coronal slices at 3.3 mm intervals progressing from posterior (left, top corner) to anterior (bottom, right corner). Although there is a significant level of image noise, it is differentiated from true lesion signal by comparison of two consecutive slices. Slices 9-14 show the positive signal from each of the three lesions. The contrast ratio of the three lesions (1.0 ml, 0.6 ml and 0.35ml) was measured to be 1.0, 0.78, 0.51, respectively (figures 15 and 16). This can be compared to the compressed planar contrast ratios of 0.43, 0.30 and 0.25 for the same phantom and lesions, respectively. This and other preliminary results indicated that better contrast can be obtained with the dedicated SPECT imaging geometry. However, in the tested pilot cases the lesions were placed in the region of the breast phantom closer to the "nipple" and therefore with less interfering tissue when imaging the suspended breast phantom. Further studies conducted with lesions in the center of the posterior aspect of the breast lacked the expected focal uptake in the reconstruction. The large cross section of breast tissue in this case eliminates the lesion signal from view and thus such lesions cannot be visualized using this modality. However, when analyzing the latter results we discovered that during the second phase of the SPECT studies the imaging geometry was not precisely controlled. Therefore, we will continue the above comparative studies to confirm our observations.

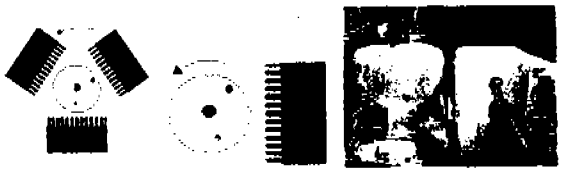

Figure 14: SPECT geometry. The left schematic shows the concept of an optimized 3-head system. In the tests the breast phantom was rotated in front of a single detector (a 4"x4" camera is shown in this example).

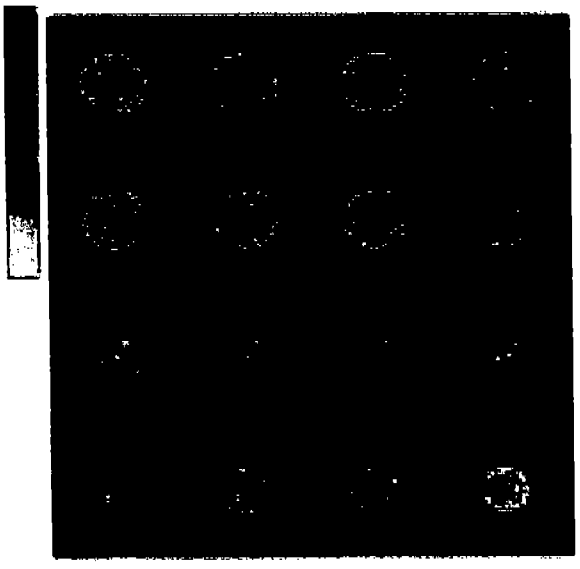

Figure 15: Example of the SPECT reconstruction results obtained with a 8"x6" imager prototype. Sixteen 3.3mm slices are shown. Left top slice #1 is the closest to the base of the breast phantom, the bottom right slice #16 is the closest to the "nipple" region. Slice #12 shows all three lesions.

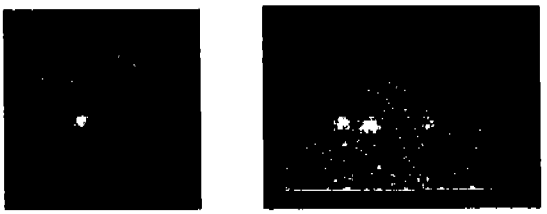

Figure 16a: Left: Reconstructed SPECT image (slice #13-bottom left in figure 15) through a 0.35ml lesion. Right: Compressed planar image of the same 0.35 ml breast lesion is on the left. Images obtained with the 8"x6" camera.

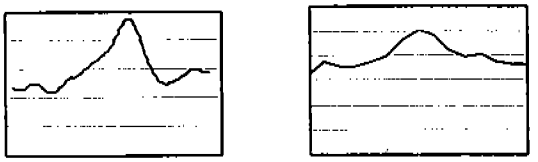

Figure 16b: Contrast differences as demonstrated by line profiles through the lesion foci for the above SPECT and planar images, respectively.

IV. CONCLUSIONS AND FUTURE PLANS

The results of the first phase of the dedicated breast imager optimization study confirm that the planar compressed geometry seems to offer the highest sensitivity for detection of all small lesions in breast, especially in its optimized form with two opposing detector heads. The dual head system would be paramount in clinical situations where lesion location is not known a priori. In the near future we will further evaluate this method of double-sided imaging with added co-registration of the two images to improve detection of asymmetrically placed small lesions but also to increase statistical validity of suspected focal hot spots by their presence in both images. We believe the added cost of the second detector head is well justified by the resulting increase in detection sensitivity. Also, in the second phase of this continuing study, a dedicated breast SPECT system with two detector heads will be built to further evaluate the SPECT imaging modality in comparison to the planar geometry.

V. ACKNOWLEDGMENTS

We thank Bicron Corporation's Mark Lowdermilk and Daniel Herr, and Hamamatsu Photonics' Edward Baro and Earl Hergert for providing us in a timely fashion with their high quality scintillator arrays and PSPMTs, respectively. Dr. Steve Meikle of the Royal Prince Alfred Hospital in Sydney, Australia, is thanked for kindly providing us with the SPECT reconstruction algorithm. We also acknowledge assistance of Dr. Marina Nerina Cinti from University of Rome "La Sapienza" in cold phantom studies.

VI. REFERENCES

[1] E. Prats, F. Aisa, M. Abos, et. al, "Mammography and ^{99m}Tc-MIBI Scintimammography in Suspected Breast Cancer", J Nucl Med, vol. 40, pp. 296-301, Feburary 1999.

[2] J. Villanueva-Meyer, M. Leonard Jr., E. Briscoe, et. al, "Mammoscintigraphy with Technetium-99-m-Sestamibi in Suspected Breast Cancer", J Nucl Med, vol. 37, pp. 926-930, June 1996.

[3] R. Taillefer, A. Robidoux, et. al, "Techtetium-99m-Sestamibi Prone Scintimammography to Detect Primary Breast Cancer and Axillary Lymph Node Involvement", J Nucl Med, vol. 36, pp. 1758-1765, July 1995.

[4] R. Pani, A. Soluri, R. Scafe, et al, "Multi-PSPMT Scintillation Camera", IEEE Trans Nucl Sci, vol., 46 pp. 702-708, 1999.

[5] M. Williams, A. Goode, Victor Galbis-Reig, et al. "Performance of a PSPMT based detector for scintimammography", Phys Med Biol, vol. 45, pp.781-800, 2000.

[6] R. Wojcik, B. Kross, D. Steinbach, A. Weisenberger, "High Spatial Resolution gamma imaging detector based on a 5" diameter Hammatsu PSPMT", IEEE Trans Nucl Sci vol 45, pp. 487-491, 1997.

[7] F. Scopinaro, R. Pani, G. De Vincentis, et al. "High-resolution scintimammography improves the accuracy of Tc-99m methoxyisobutylisonitrile scintimammography: use of a new dedicated gamma camera". Eur J Nucl Med vol. 26, pp.1279-1288, 1999.

[8] C. Maini, F. de Notaristefani,, et. al, "Tc-MIBI Scintimammography Using a Dedicated Nuclear Mammograph", J Nucl Med vol. 40, pp. 46-51, January 1999.

[9] G. Gruber, W. Moses, S. Derenzo, "A Discrete Scintillation Camera Module Using Silicone Photodiode Readout", IEEE Trans Nucl Sci vol NS-45, pp. 1063-1068, 1998.

[10] M. Singh, E. Mumcuoglo, "Design of CZT Based Breast SPECT System", IEEE Conference, 1998.

[11] C. Thompson, K. Murthy, et al, "Feasibility study for positron emission mammography", Med Phys vol. 21 pp. 592-538, April 1994

[12] R. Raylman, S. Majewski, R. Wojcik, et al, "Positron Emission Mammography-Guided Stereotatic Biopsy", J Nucl Med., Vol. 40, p116, January 1999.

[13] R. Freifelder, J. Karp, "Dedicated PET scanners for breast imaging", Phys Med Biol vol. 42, p.1012, 1997.

[14] N. Doshi, S. Yiping, et al, "Design and evaluation of an LSO PET detector for breast cancer imaging", Excepted for publication Medical Physics 2000.

[15] H. Wang, C. Scarfone, K. Greer, et. al, "Prone Breast Imaging Using Vertical Axis-of-Rotation (VAOR) SPECT Systems: An Initial Study", IEEE Trans Nucl Sci, vol. 44, pp.1271-1276, 1997.

[16] R. Tiling, K. Tatsch, et. al, "Technetium-99m-Sestamibi Scintimammography for the Detection of Breast Carcinoma: Comparison Between Planar and SPECT Imaging", J Nucl Med vol. 39, pp. 849-855, May 1998.

[17] R. Brem, S. Majewski, J. Links, et al, "Radionuclide Imaging of the Breast Using a Small Field of View, High Resolution Breast Specific Gamma Camera", Poster RSNA meeting, November 1999.

[18] R. Brem, J. Schoonjans, "Detection of Breast Cancer with a Novel, High Resolution Breast Specific Gamma Camera: Preliminary Results", Submitted for publication in Radiology 2000.

[19] Hamamatsu Corporation, Bridgewater, NJ

[20] Bicron Corporation (presently: Saint Gobain Crystals and Detectors), Newbury, OH.

[21] Sparrow Corporation, Starkville, MS

[22] Thermo Electron - Tecomet, http://www.tecomet.com.

[23] F.Adams, R. Dams, Applied Gamma-Ray Spectrometry, New York: Pergamon Press, 1970, pp. 1-60.

[24] K. Murthy, D. Jolly M. Aznar, et al, "Quantification in positron emission mammography with planar detectors: contrast resolution measurements using a custom breast phantom and novel spherical hot-spots", IEEE Trans Nucl Sci vol. 46, pp. 1292-1296, 1998.

[25] Data Spectrum Inc., Hillsborough, NC.

[26] F. Wackers, D.Bertman et al, "Technetium-99m Hexakis 2-Methoxyisobutyl isonitrile: Human Biodistribution, Dosimetry, Safety, and Preliminary Comparison to Thallium-201 for Myocardial Imaging", J Nuc Med, vol. 30, pp. 301-311, March 1989

[27] J. Maublant, M DeLatour, et al, "Technetium-99m-Sestamibi Uptake in Breast Tumor and Associated Lymph Nodes", J Nuc Med vol. 37, pp. 922-925, 1996

[28] Hilger Crystals Ltd., England.

[29] I.N. Weinberg, R. Pani, et al, "Small Lesion Visualization in Scintimammography", IEEE Trans Nuc Sci, vol 44, no 3, June 1997.

[30] Dr. Roberto Pani, University of Rome "La Sapienza", private communication.